Modeling Radiation Damage to Pixel Sensors in the ATLAS Detector

Lorenzo Rossini[*]**, on behalf of the ATLAS Collaboration**

Universita´ degli studi di Milano, INFN sezione di Milano, Italy
E-mail: lorenzo.rossini@unimi.it

Silicon pixel detectors are at the core of the current and planned upgrade of the ATLAS detector at the Large Hadron Collider (LHC). As the closest detector components to the interaction point, these detectors will be subjected to a significant amount of radiation over their lifetime: prior to the High-Luminosity LHC (HL-LHC), the innermost layers will receive a fluence in excess of $10^{15} n_{\rm eq}/{\rm cm}^2$ and the HL-HLC detector upgrades must cope with an order of magnitude higher fluence integrated over their lifetimes. Simulating radiation damage is critical in order to make accurate predictions for current and future detector performance that will enable searches for new particles and forces as well as precision measurements of Standard Model particles such as the Higgs boson. A digitization model that includes radiation damage effects to the ATLAS pixel sensors and considers both planar and 3D sensor designs, is presented. In addition to the thorough description of the setup, predictions for basic pixel cluster properties on leakage currents, depletion voltage, charge collection efficiency, and Lorentz angle are compared with LHC proton-proton collision data.

---

[*]Speaker.

1. The ATLAS Pixel Detector and Radiation Damage effects

The ATLAS [1] Pixel Detector [2] is the innermost component of the Inner Detector. It consists of four barrel layers and three disk layers per end cap. The barrel layers are composed of n^+-in-n planar oxygenated silicon sensors and n^+-in-p 3D pixel sensors. These sensors cover a total active area of 1.88 m^2 with a total of 92.4 million pixels. Its coverage goes up to $|\eta| < 2.5$[1], while it covers the full azimuthal angle (ϕ).

The innermost layer, the Insertable B-Layer (IBL) [3, 4], is located at just 3.3 cm from the beam pipe and is made of pixels of 50×250 μm^2 in size and 200 μm thick, while in the region with high $|z|$ of the IBL there are the 3D pixel sensors of 50×250 μm^2 in size and 230 μm thick. The other barrel layers are respectively at 5.05 cm (B-Layer), 8.85 cm (Layer 1), and 12.55 cm (Layer 2) from the beam pipe and consist of pixels of 50×400 μm^2 in size and 250 μm thick. The IBL was installed in ATLAS in May 2014 before the start of LHC Run 2, while the other three layers have been there since the beginning of Run 1. The IBL modules are tilted by 14° in the azimuthal direction, and the other pixel layers by 10°, achieving overlap in the active area and assuring a full acceptance in ϕ.

The IBL received a total fluence of $\sim 1 \times 10^{15}\, n_{\rm eq}/{\rm cm}^2$ by the end of Run 2 (corresponding to a luminosity delivered by the LHC of 159 fb^{-1}), while a total fluence of $1.8 \times 10^{15}\, n_{\rm eq}/{\rm cm}^2$ is estimated by the end of Run 3 in 2023 (with a total estimated integrated luminosity of 300 fb^{-1}). The other three layers have received lower fluences: $4.6 \times 10^{14}\, n_{\rm eq}/{\rm cm}^2$ for the B-Layer, $2.1 \times 10^{14}\, n_{\rm eq}/{\rm cm}^2$ for Layer-1, and $1.3 \times 10^{14}\, n_{\rm eq}/{\rm cm}^2$ for Layer-2. Figure 1 shows the fluence received by the four layers as a function of the number of days since the start of Run 2 .

The remainder of this contribution will present the details of a new digitizer that accounts for effects due to radiation damage. Section 2 presents the model used and each component used, and Section 3 presents the results of the simulation compared with data from Run 2.

2. Digitizer Model

Charged particles crossing a sensor create electron-hole pairs that travel towards the electrodes due to the combined effects of the electric and magnetic fields. They induce a signal in the collecting electrodes where they are converted to digital signals and sent from the front ends to the detector readout system.

In simulations, energy deposits are obtained from Geant4 [5], a software that evaluates the trajectories of particles inside the detector and their interaction with the material, and whose output is a list of energy deposits and their position in the sensitive material, called *hits*. These hits are then transformed into digital signals in a step called *digitization*. Radiation damage effects are inserted in this step in a software based on AllPix [6]. This is a tool which allows an easy and fast comparison between data and simulation, and was used to prove the validity of the radiation damage model. Afterwards, the model was also implemented in the ATLAS common software Athena, in

---

[1]ATLAS uses a right-handed coordinate system with its origin at the nominal interaction point (IP) in the centre of the detector and the z-axis coinciding with the axis of the beam pipe. The x-axis points from the IP towards the centre of the LHC ring, and the y-axis points upward. Cylindrical coordinates (r, ϕ) are used in the transverse plane, ϕ being the azimuthal angle around the z-axis. The pseudorapidity is defined in terms of the polar angle θ as $\eta = \ln\tan(\theta/2)$.
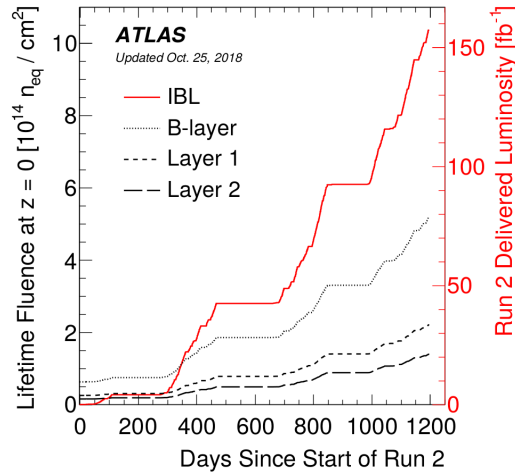
Figure 1: Estimates of the lifetime fluence experienced by the four layers of the current ATLAS pixel detector as a function of time since the start of Run 2 (June 3, 2015) at $z \sim 0$. The IBL curve represents both the fluence on the IBL (left axis) as well as the delivered integrated luminosity in Run 2 (right axis). From Ref. [7].

order to exploit the full-geometry description of the ATLAS detector, and check what the effects on physical quantities would be. However, in both cases the structure of the main algorithm to evaluate the effects of the radiation damage is the same, while there are some differences in how some maps and geometry setting are initialized.

Overview   The software is initialized by loading the geometry of the sensor (thickness, pitch, tilt) and Geant4 generates the energy hits. Then all the parameters needed are loaded: fluence, trapping time for electrons and holes, temperature, and magnetic field strength. In this step a number of lookup tables are also loaded: Ramo potential, electric field maps, and Lorentz angle maps.
The energy deposits of Geant4 are then converted into electron-hole pairs; the energy needed is $\sim 3.6\,\text{eV}$ for a pair. These charge carriers are then drifted towards the opposite electrodes using the information in the tables previously loaded. For each charge the probability of being trapped is then calculated. If the charge is trapped, the signal induced in the neighboring pixels is then evaluated using the Ramo potential.
The different inputs are described in the following paragraphs.

Fluence   Fluence is proportional to the delivered luminosity. In order to match the data to the correct simulation it is then important to know the conversion factor between fluence and luminosity. This is obtained by comparing the prediction of the leakage current with data. Figure 2 (left) shows the predicted leakage current compared with data during Run 2. Figure 2 (right) shows the conversion factor from luminosity to fluence for the IBL, as a function of z, compared with predictions with Pythia8+FLUKA [8, 9] and Pythia+Geant4. From a comparison with the different simulation an error of 15 % is assumed on this conversion factor.

Electric Field   The electric field strength for unirradiated sensors varies linearly with the depth
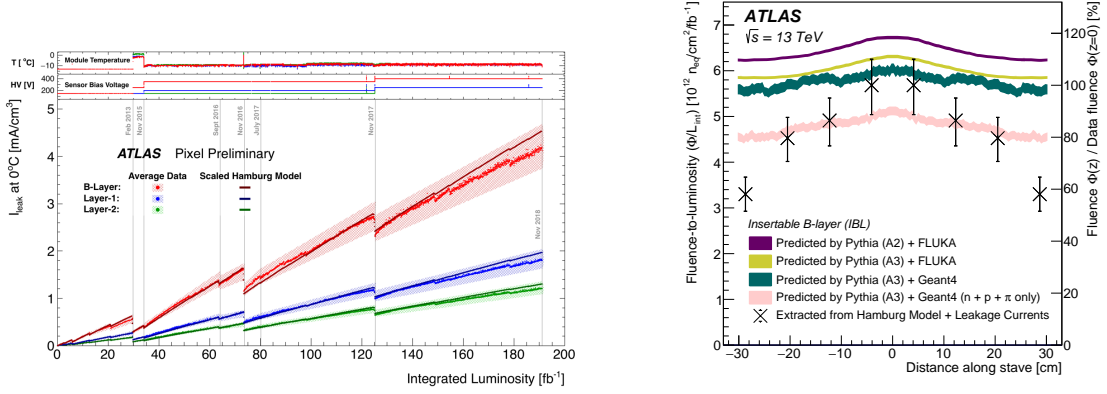
Figure 2: Left: Average measured leakage current data of a representative sample of modules in the ATLAS Pixel Detector barrel layers over the full period of operation. The leakage current data are normalized to $0°C$; the average module sensor temperature is shown in the top panel. From Ref. [10]. Right: The fluence-to-luminosity conversion factors (extracted from leakage current fits), as a function of z, compared with the Pythia+FLUKA and Pythia+Geant4 predictions. From Ref. [11].

of the sensor. However the change in doping inside the bulk due to the radiation damage changes the profile of the field. The electric field strength for irradiated sensors are simulated with software based on TCAD technologies. The radiation damage models used were the Chiochia model [12] for planar sensors and the Perugia model [13] for the 3D sensors.

Lorentz angle The presence of a magnetic field deviates the path of the charge carriers from straight lines. The Lorentz angle (θ_L) is defined as the angle between the drift direction and the electric field. In a given point inside the bulk of the sensor the Lorentz angle is given by

$$\tan\theta_L(z_i, z_f) = \frac{rB}{|z_f - z_i|} \int_{z_i}^{z_f} \mu(E(z))dz,$$

where μ is the mobility, and $z_{i/f}$ is the initial/final position, r is the Hall scattering factor, B is the magnetic field, and $E(z)$ is the electric field as a function of the position. From this equation it is possible to see that if the electric field changes, so too does the Lorentz angle, due to the dependency of the mobility on the electric field. In the digitizer code the Lorentz angle maps are saved at the beginning for each geometry and condition setup (fluence, bias voltage, and temperature).

Charge Trapping The charge carriers are considered trapped if their time to reach the electrodes is larger than a random time distributed as an exponential with mean value $1/(\Phi\beta)$, where β is the trapping constant, and Φ the fluence. This constant is set at the beginning of the digitizer, and it is taken from literature. From different measurements, β has been found to depend on the type of irradiation, the temperature, and the annealing history, and also on whether the charge carrier is an electron or a hole. In the digitizer an average of different measurements is used, mainly from references [14, 15, 16]. The values used were:

$$\beta_e = (4.5 \pm 1.5) \times 10^{-16} \text{cm}^2/\text{ns},$$
$$\beta_h = (6.5 \pm 1.5) \times 10^{-16} \text{cm}^2/\text{ns}.$$

The uncertainties were chosen in order to cover the differences between the measurements in the references used.

Ramo potential and induced charge   Even if the charges are trapped inside the bulk of the sensor, they still induce a charge on the electrodes that can be analytically calculated, by using the Shockley-Ramo theorem [17]. The induced signal of a charge q moving from the position $\vec{x}_i$ to the position $\vec{x}_f$ is:

$$Q_{\text{induced}} = -q[\phi_{\text{w}}(\vec{x}_{\text{f}}) - \phi_{\text{w}}(\vec{x}_{\text{i}})],$$

where ϕ_{w} is the Ramo potential $\vec{E}_{\text{w}} = -\nabla\phi_{\text{w}}$. The Ramo potential depends only on the geometry of the electrodes, and therefore it is evaluated in advance. In the digitizer the Ramo maps are loaded in the initialization process, and are used in each loop whenever a charge is trapped to estimate the induced charge in all the pixels in a 3×3 matrix around the closest pixel to the trapping position. These maps are evaluated with TCAD in order to solve the Poisson equation. Figure 3 shows the Ramo potential of a quarter of an IBL planar sensor.
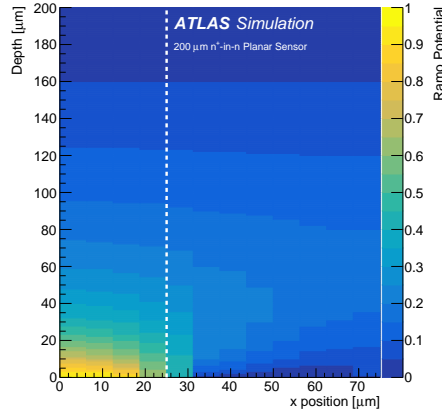
Figure 3: Ramo potential maps of a quarter of an ATLAS IBL planar module in the $z-x$ plane. The dashed vertical line (at 25 μm) indicates the edge of the primary pixel. From Ref. [11].

3. Validation with Data

Standalone simulations with Allpix are used to predict the evolution with fluence of the performance of the detector. This allows the radiation damage model to be validated using collision data, as well as to predict future performance and to plan changes to operating conditions in order to maintain a high detection efficiency. Simulation results are compared to data from Run 2 collected with the ATLAS IBL detector. During this time the bias voltage was increased to cope with radiation damage: the IBL sensors have operated at 80 V in 2015, 150 V in 2016, 350 V in 2017, and 400 V in 2018.

Charge Collection Efficiency   One important observable to monitor is the collected charge, which is reported as the most probable value of the charge cluster distribution. This is expressed in Time over Threshold (ToT). The charge collection efficiency (CCE) is defined as the ratio of the most probable value at a certain fluence with respect to the value for unirradiated sensors. The charge collection efficiency as a function of the delivered luminosity for central ($|\eta| < 0.8$) IBL modules is shown in figure 4 (left). The agreement between data and simulation is good within

the simulation uncertainties. Systematic uncertainties come from the variation of the fundamental parameters in the radiation model used to compute the electric field profile, and from the variations of the trapping constants.

The evolution of the collected charge as a function of the bias voltage for data from the end of 2017 and 2018, and simulation for two fluences, corresponding respectively to the end of 2017 and end of 2018 for IBL modules, is shown is figure 4 (right) . The data are taken in special runs where scans of bias voltages were performed. Again the simulation is in good agreement with data in both trend and absolute value.
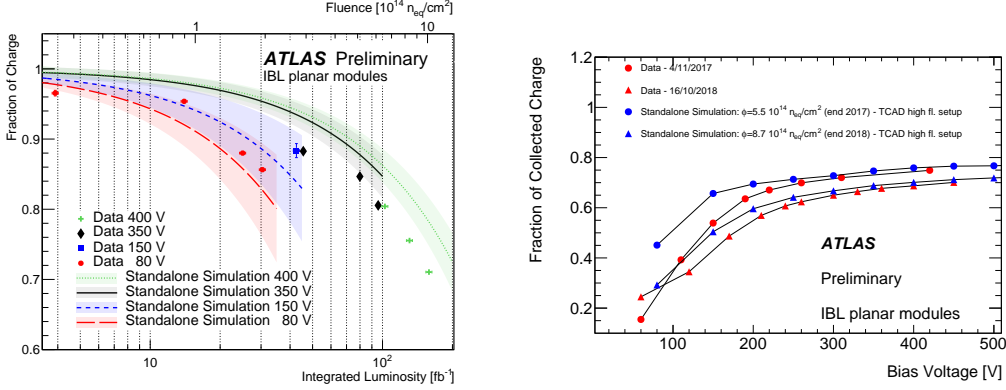
Figure 4: Left: Charge collection efficiency as a function of luminosity. Right: Most probable value of ToT as a function of bias voltage. From Ref. [18].

Lorentz angle   Another important parameter to monitor is the Lorentz angle, since it has a direct impact on the cluster size. The Lorentz angle is determined by performing a fit to the transverse cluster size F as a function of the incidence angle of the associated track using the following functional form:

$$F(\alpha) = [a \times |\tan\alpha - \tan\theta_L| + b/\sqrt{\cos\alpha}] \otimes G(\alpha|\mu = 0, \sigma),$$

where α is the incidence angle with respect to the normal direction of the sensor in the plane perpendicular to the magnetic field. The parameter θ_L is the fitted Lorentz angle, G is a Gaussian probability distribution evaluated at α with mean 0 and standard deviation σ, and a and b are two additional fit parameters related to the depletion depth and the minimum cluster size, respectively. An example input to the fit is shown in Figure 5 (right). Figure 5 (left) instead shows the evolution of the Lorentz angle during 2017 compared with the prediction from the Allpix simulations. Here the simulation points are fitted with a straight line, where the offset is fixed so that it matches the one from the data. The overall normalisation of the simulation prediction is highly sensitive to the radiation damage model parameters, but the increasing trend is robust.

Error bands account for all the systematic variations. For each one a linear fit is done, and the error is defined as the sigma of the distribution of the slopes. The increase in data is well described by the simulations.
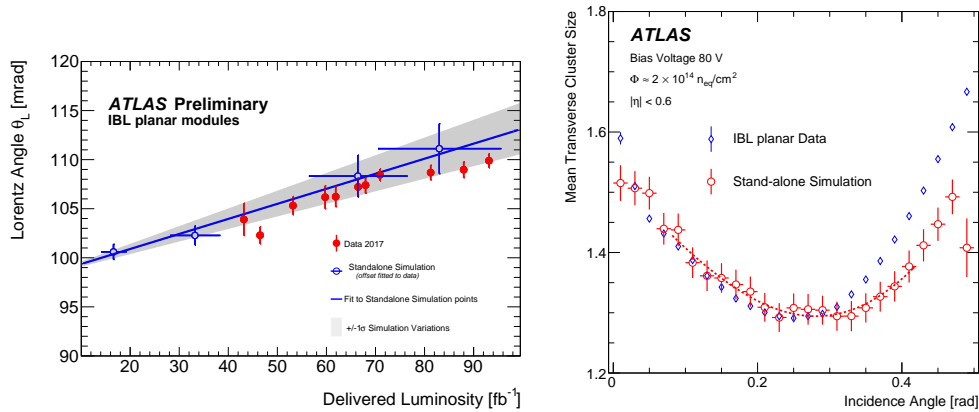
Figure 5: Left: The evolution of the Lorentz angle (θ_L) during 2017 compared with simulations from Allpix using the Chiochia model. From Ref. [19]. Right: The mean transverse cluster size versus transverse incidence angle near the end of the 2016 run ($\sim 2 \times 10^{14}$ n_{eq}/cm^2) with a bias voltage of 80 V. From Ref. [11].

4. Conclusion

Radiation damage effects are already visible in the ATLAS Pixel Detector and need to be taken into account in the Monte Carlo simulations in order to be prepared for Run 3 at the LHC. A digitizer that models the effects of the radiation damage has been presented. It is based on TCAD simulations with effective traps in the silicon bulk that model the changes in the electric field profile. Comparison of the simulations with data shows good agreement. Results of the simulation were used to help to make decisions that ensure good online and offline performance of the ATLAS Pixel Detector, and to guide the design of the future detector at the HL-LHC.

References

[1] ATLAS Collaboration, *The ATLAS Experiment at the CERN Large Hadron Collider*, JINST **3** (2008) S08003. doi:10.1088/1748-0221/3/08/S08003

[2] G. Aad, et al., *ATLAS pixel detector electronics and sensors*, JINST 3 (2008) P07007. doi:10.1088/1748-0221/3/07/P07007.

[3] ATLAS Collaboration, *ATLAS Insertable B-Layer Technical Design Report*, Tech. Rep. CERN-LHCC-2010-013. ATLAS-TDR-19 (Sep 2010). URL https://cds.cern.ch/record/1291633

[4] B. Abbott, et al., *Production and Integration of the ATLAS Insertable B-Layer*, JINST 13 (05) (2018) T05008. arXiv:1803.00844, doi:10.1088/1748-0221/13/05/T05008.

[5] S. Agostinelli, et al., *GEANT4: A Simulation toolkit*, Nucl. Instrum. Meth. A506 (2003) 250-303. doi:10.1016/S0168-9002(03)01368-8.

[6] J. Idarraga, M. Benoit, *Generic Geant4 implementation for pixel detectors, The AllPix Simulation Framework* (2006) [twiki.cern.ch:AllPix].

[7] ATLAS Collaboration, *Radiation damage in 2015-2017*, https://atlas.web.cern.ch/Atlas/GROUPS/PHYSICS/PLOTS/PIX-2018-005/

6

[8] T. Sjostrand, et al., *An Introduction to PYTHIA 8.2*, Comput. Phys. Commun. 191 (2015) 159, arXiv: 1410.3012 [hep-ph], doi: 10.1016/j.cpc.2015.01.024 .

[9] A. Ferrari, et al., *FLUKA: A multi-particle transport code (program version 2005)*, CERN Yellow Reports: Monographs, Geneva: CERN, 2005, url: https://cds.cern.ch/record/898301

[10] ATLAS Collaboration, *Measurements and Predictions of Pixel Detector Leakage Current*, https://atlas.web.cern.ch/Atlas/GROUPS/PHYSICS/PLOTS/PIX-2018-008/

[11] ATLAS Collaboration, *Modelling radiation damage to pixel sensors in the ATLAS detector*, JINST, 14 (2019), 06, P06012, arXiv:1905.03739, doi 10.1088/1748-0221/14/06/P06012, CERN-EP-2019-061

[12] V. Chiochia, et al., *A Double junction model of irradiated silicon pixel sensors for LHC*, Nucl. Instrum. Meth. A568 (2006) 51-55. arXiv:physics/0506228, doi:10.1016/j.nima.2006.05.199.

[13] F. Moscatelli, et al., *Combined Bulk and Surface Radiation Damage Effects at Very High Fluences in Silicon Detectors: Measurements and TCAD Simulations*, IEEE Trans. Nucl. Sci., 63, (2016), 2716-2723, doi 10.1109/TNS.2016.2599560.

[14] O. Krasel, et al., *Measurement of trapping time constants in proton-irradiated silicon pad detectors*, IEEE Trans. Nucl. Sci., 51 (2004), 3055-3062, doi 10.1109/TNS.2004.839096.

[15] G. Kramberger, et al., *Effective trapping time of electrons and holes in different silicon materials irradiated with neutrons, protons and pions.* Nucl. Instrum. Meth., A481 (2002), 297, doi 10.1016/S0168-9002(01)01263-3.

[16] G. Alimonti, et al., *A study of charge trapping in irradiated silicon with test beam data*, 2003, ATL-INDET-2003-014, ATL-COM-INDET-2003-020, CERN-ATL-INDET-2003-014

[17] S. Ramo, *Currents Induced by Electron Motion*, 1939, Proceedings of the IRE, volume 27, pages 584-585, doi: 10.1109/JRPROC.1939.228757.

[18] ATLAS Collaboration, *Charge Collection Efficiency as a function of integrated luminosity*, https://atlas.web.cern.ch/Atlas/GROUPS/PHYSICS/PLOTS/PIX-2017-004.

[19] ATLAS Collaboration, *Radiation damage to the ATLAS pixel*, https://atlas.web.cern.ch/Atlas/GROUPS/PHYSICS/PLOTS/PIX-2017-005/